Research Paper

CFD simulation of biomass steam gasification in a fluidized bed based on a multi-composition multi-step kinetic model

Qitai Eri [a], Jing Peng [a], Xinjun Zhao [a,b,*]

[a] School of Energy and Power Engineering, Beihang University, Beijing 100191, China
[b] The 41st Research Institute, The Sixth Academy of CASIC, Hohhot 010010, China

HIGHLIGHTS

- Novel multi-composition multi-step steam gasification kinetic model is proposed.
- Detailed pyrolysis scheme is adopted in the kinetic model.
- Proposed kinetic model can predict tar composition.
- Effects of gasification parameters on simulation results are reported.

ARTICLE INFO

ABSTRACT

In the present study, a novel kinetic model for biomass steam gasification process along with a detailed multi-composition multi-step pyrolysis scheme is developed, which can predict tar composition. In addition, based upon the two-fluid model and kinetic theory of granular flow, simulations were carried out. A comparison between the simulation results and experimental data was made. The results showed that the proposed model produced satisfactory results. The effects of gasification parameters on non-condensable gas composition, tar content, tar composition, and char yield were also studied. The study showed that the gasification temperature has an evident influence on simulation results, while the effect of steam to biomass ratio (SBR) on simulation results was not obvious.

© 2017 Elsevier Ltd. All rights reserved.

1. Introduction

Biomass gasification is a thermochemical conversion process, which can convert biomass into combustible gases, such as H_2 and CO. Due to its capability of handling a variety of biomass feedstocks and high energy conversion efficiency, biomass gasification has gained worldwide attention. Additionally, the produced gases can be used either as a fuel in daily life or for electric generation in power plants. Due to good mixing and contact between the gas and solid phases, bubbling fluidized bed is commonly used in the gasification process [1,2].

During gasification, pyrolysis, heterogeneous, and homogeneous gas phase reactions take place, which involve both heat and mass transfer processes. Because of its inherent complexity, modeling for the prediction of gasification performance is still in an early research phase [3]. Therefore, more accurate mathematical models need to be established to study the composition and distribution of produced gas (syngas). In the simulation of gasification, kinetic models [4,5] consider both the reaction mechanisms and reactor hydrodynamics, which make them suitable and accurate to represent the gasification process. Due to recent advances in computational capabilities and numerical algorithms, simulations based on computational fluid dynamics (CFD) have become a useful method to study the gasification behavior in a bubbling fluidized bed reactor [6]. In the CFD simulation of a fluidized bed, the two-fluid model (TFM) is often used for modeling gasification due to its exceptional computational efficiency. In this model, the gas and solid phases are treated as interpenetrating continua, however the equations of continuity, momentum, and energy of the solid phase are similar to those of the gas phase.

The first step of the gasification process is the pyrolysis, while the products of pyrolysis are a mixture of non-condensable gases, tar (macromolecular gases) and char [7]. Hence, the pyrolysis model is important in gasification simulations. More detailed the

* Corresponding author at: School of Energy and Power Engineering, Beihang University, Beijing 100191, China.
E-mail addresses: eriqitai@buaa.edu.cn (Q. Eri), pengjing15@buaa.edu.cn (J. Peng), kunpengzhao@buaa.edu.cn (X. Zhao).

pyrolysis model is, better will be the simulation results. Some researchers [8,9] assumed that the pyrolysis was an instantaneous process, which was completed at the feeding position. Due to these assumptions, based upon the experimental data, the pyrolysis compositions were used as the input parameters in the gasification simulation. Other researchers used different models to study the pyrolysis process. Liu et al. [10] and Ku et al. [11] used one-step global-reaction scheme to simulate the biomass pyrolysis, which only produced volatile gases and char. Ismail et al. [12] used one-step global model to study the pyrolysis process, in which secondary pyrolysis reactions of tar was involved. Xue et al. [13] and Gerber et al. [14] adopted a global parallel kinetic model, which included three competitive reactions to demonstrate the pyrolysis process, and involved products of char and tar.

In most of the previous studies on gasification simulations, biomass is generally represented by a lumped structural formula. In fact, biomass compositions mainly comprise of cellulose, hemicellulose, and lignin, whereas different compositions of biomass yield different product components in different proportions during pyrolysis [15]. Hence, the effect of composition on pyrolysis products cannot be reflected when the lumped structural formula is adopted. Moreover, in the global pyrolysis model, tar is represented in lumped formula, due to which, the detailed composition of tar cannot be determined. Therefore, the universality of gasification model, which represents biomass as a lumped structural formula and is based on global pyrolysis scheme, is limited.

In biomass gasification, the content of hydrogen and heating value of syngas are very high, when steam is used as the gasifying agent. Due to this reason, steam gasification has received a lot of research attention [16,17]. In this study, a multi-composition multi-step steam gasification kinetic model, which relates to the biomass composition, is proposed along with detailed pyrolysis scheme that can predict tar composition of syngas. Furthermore, Fluent 15.0 software is used to carry out simulations based on two-fluid model along with the kinetic theory of granular flow. A comparison between the simulation results and experimental data is also drawn. In addition, the effects of gasification parameters on simulation results are also analyzed and reported in this work.

2. Model description

2.1. Chemical kinetic model

2.1.1. Pyrolysis model

The biomass mainly consists of cellulose, hemicellulose, and lignin, whereas the primary pyrolysis kinetic scheme for various biomass compositions is shown in Table 1 [18,19]. In simulation, the heat of reactions is needed for pyrolysis reactions, and the corresponding data can also be found in the same reference [19]. Some research [20] has been conducted to study the possible interactions between the biomass compositions. The experimental results are obtained from the mixed samples of different biomass compositions while the estimated values are obtained from the results of the individual component, so the difference between the experimental and estimated yields indicates the interaction. The result shows that the cellulose-hemicellulose interaction is not significant. Meanwhile, the cellulose-lignin interaction is stronger than the cellulose-hemicellulose interaction. However, it is difficult to obtain the quantitative influence. Hence, in most studies [21–23], possible interactions between the biomass compositions are neglected. In this study, the possible interactions between the biomass compositions are also neglected in pyrolysis process.

In Table 1, *Cell* and *HCell* are the cellulose and hemicellulose, respectively, whereas, *LignC*, *LignH*, and *LignO* are various types of lignin with the characteristic of being richer in carbon, hydrogen, and oxygen, respectively. Other components are the intermediate products, which are obtained in the primary pyrolysis stage. *CellA* is also an intermediate product, which represents the "active" cellulose obtained from cellulose. Cellulose, hemicellulose, lignin, "active" cellulose, and char constitute the solid phase, while the other components belong to the gas phase. The heat of reaction is obtained from the literature [24]. In these primary pyrolysis reactions, all of the gases except H_2, CH_4, CO, CO_2, C_2H_4, and H_2O contribute to the tar composition. The pyrolysis reactions are modeled with the first-order Arrhenius kinetics and the reaction rate constant is expressed using Eq. (1).

$$k_e = A_e \cdot \exp[-E/(RT)] \tag{1}$$

where k_e is the reaction rate constant (1/s), A_e is the pre-exponential factor (1/s). E is the activation energy (kJ/mol). T is the temperature (K), and R is the universal gas constant with the value of 8.314 J/(mol·K).

The tar content in syngas primarily depends on the gasification temperature [25]. The primary tar is generally generated in the pyrolysis stage and decomposes further at a temperature higher than 500 °C [26]. The secondary pyrolysis reactions for tar are quite complicated, and their reaction mechanism is not well understood. Based on the cracking reactions of tar proposed by Blondeau et al. [27] and the hypothetical values for A and E [19], the products of secondary pyrolysis reactions include non-condensable gases and char, whereas the reaction scheme for this stage is shown in Table 2.

Table 1
Kinetic scheme used for primary pyrolysis reactions.

Reactions		A (1/s)	E (kJ/mol)
R1	Cell → 5H_2O+6C	8×10^7	125.5
R2	Cell → CellA	8×10^{13}	192.5
R3	CellA → LVG	$4T$	41.8
R4	CellA → 0.16CO_2 + 0.23CO + 0.9H_2O + 0.1CH_4 + 0.61C + 0.25 $C_6H_6O_3$ + 0.2CH_3COCH_3 + 0.2CH_3HCO + 0.25$C_2H_2O_2$ + 0.95HAA	1×10^9	133.9
R5	HCell → 0.4HCell1 + 0.6HCell2	1×10^{10}	129.7
R6	HCell1 → 0.75H_2 + 0.8CO_2 + 1.4CO + 0.5CH_2O	3×10^9	113.0
R7	HCell1 → Xylan	$3T$	46.0
R8	HCell2 → CO_2+0.5CH_4 + 0.25C_2H_4 + 0.8CO + 0.8H_2 + 0.7CH_2O + 0.25CH_3OH + 0.125C_2H_5OH + 0.125H_2O + C	1×10^{10}	138.1
R9	LignC → 0.35LignCC + 0.1pCoumaryl + 0.08C_6H_5OH + 0.41C_2H_4 + H_2O+0.495CH_4 + 0.32CO + CO+H_2 + 5.735C	4×10^{15}	202.9
R10	LignH → LignOH + CH_3COCH_3	2×10^{13}	156.9
R11	LignO → LignOH + CO_2	1×10^9	106.7
R12	LignCC → 0.3pCoumaryl + 0.2C_6H_5OH + 0.35Acrylic-acid + 0.7H_2O + 0.65CH_4 + 0.6C_2H_4 + 1.8CO + H_2+6.4C	5×10^6	131.8
R13	LignOH → Lign+H_2O + CH_3OH+0.45CH_4 + 0.2C_2H_4 + 2CO + 0.7H_2 + 4.15C	3×10^8	125.5
R14	Lign → Lumped-phenol	$8T$	50.2
R15	Lign → H_2O+2CO + 0.2CH_2O + 0.4CH_3OH + 0.2CH_3HCO+0.2 CH_3COCH_3 + 0.6CH_4 + 0.65C_2H_4 + 0.5H_2 + 5.5C	1.2×10^9	125.5

Table 2
Secondary pyrolysis reactions for tar.

Reactions		A (1/s)	E (kJ/mol)
R16	$C_6H_6O_3 \rightarrow 3CO + 1.5C_2H_4$	4.28×10^6	108.0
R17	$CH_3COCH_3 \rightarrow 0.5CO_2 + 0.5H_2 + 1.25C_2H_4$	4.28×10^6	108.0
R18	$pCoumaryl \rightarrow CO_2 + 2.5C_2H_4 + 3C$	4.28×10^6	108.0
R19	$C_6H_5OH \rightarrow 0.5CO_2 + 1.5C_2H_4 + 2.5C$	4.28×10^6	108.0
R20	$Xylan \rightarrow 2CO_2 + H_2 + 1.5C_2H_4$	4.28×10^6	108.0
R21	$LVG \rightarrow 2.5CO_2 + 1.5H_2 + 1.75C_2H_4$	4.28×10^6	108.0
R22	$HAA \rightarrow 2CO + 2H_2$	4.28×10^6	108.0
R23	$C_2H_2O_2 \rightarrow 2CO + H_2$	4.28×10^6	108.0
R24	$Lumped\text{-}phenol \rightarrow 2CO_2 + 3C_2H_4 + 3C$	4.28×10^6	108.0
R25	$Acrylic\text{-}acid \rightarrow CO_2 + C_2H_4$	4.28×10^6	108.0

2.1.2. Heterogeneous reactions

After pyrolysis, the char will continue to react with the gases. For pure steam gasification process, the char heterogeneous reactions in gasification model are given by Reactions R26 – R28, which are shown in Table 3. Reactions R26 – R28 represent Boudouard reaction, steam gasification reaction, and methanation reaction, respectively. As mentioned in some previous studies [28], the kinetic scheme for the heterogeneous reactions of char has not been fully understood, and therefore, the available kinetic parameters have significant inherent deviations. However, it is generally agreed that the rate of methanation reaction is far slower than that of the steam gasification [13,14]. The rate expressions and kinetic parameters for the heterogeneous reactions are also summarized in Table 3 [14], whereas the corresponding reaction rate constant is expressed using Eq. (2).

$$k_e = A_e \cdot T_s \cdot \exp[-E/(RT)] \qquad (2)$$

where T_s is the temperature of char (K), whereas rest of the terms carry the same meaning and units as explained below Eq. (1).

The reaction rate for heterogeneous reactions is introduced into the gasification model by using the user-defined functions (UDF) method.

2.1.3. Homogeneous gas phase reactions

For pure steam gasification, the homogeneous gas phase reactions are given by Reactions R29 – R31, as given in Table 4. In homogeneous gas phase reactions, just water gas shift reaction (Reaction R31) is considered as a reversible reaction. The volumetric reaction rate model is used in the simulation, and the kinetic parameters [16,29,30] are summarized in Table 4.

The effects of both the kinetic rate and the turbulent mixing are considered when modeling the homogeneous gas phase reactions, and the finite rate/eddy dissipation model is adopted.

The eddy dissipation model is a turbulence-chemistry model, according to which the reaction rate is given by Eq. (3).

$$r_{Eddy\text{-}dissipation} = v_{i,r} M_{w,i} A \rho \frac{\varepsilon}{k} \min \left[\min_R \left(\frac{Y_R}{v_{R,r} M_{w,R}} \right), B \frac{\sum_p Y_p}{\sum_j^N v_{j,r} M_{w,j}} \right] \qquad (3)$$

where $v_{i,r}$ is the stoichiometric coefficient for reactant i in reaction r, $v_{R,r}$ is the stoichiometric coefficient for reactant R in reaction r. $v_{j,r}$ is

Table 4
Kinetic parameters for the homogeneous gas phase reactions.

Reactions		Reaction rate
R29	$CH_4 + H_2O \rightarrow CO + 3H_2 - $ 206 kJ/mol	$r = 3.0 \times 10^5 \cdot \exp(-15042/T) C_{CH_4} C_{H_2O}$
R30	$C_2H_4 + 2H_2O \rightarrow 2CO + 4H_2 - $ 212 kJ/mol	$r = 3100.5 \cdot \exp(-15000/T) C_{C_2H_4} C_{H_2O}^2$
R31	$CO + H_2O \leftrightarrow CO_2 + H_2 + 41$ kJ/mol	$r_+ = 7.68 \times 10^{10} \cdot \exp(-36640/T) C_{CO}^{0.5} C_{H_2O}$ $r_- = 6.4 \times 10^9 \cdot \exp(-39260/T) C_{CO_2} C_{H_2}^{0.5}$

the stoichiometric coefficient for product j in reaction r, y_p is the mass fraction of any product species, and y_R is the mass fraction of a particular reactant. Furthermore, M, k, and ε are the molecular weight, turbulence kinetic energy, and dissipation rate, respectively. Additionally, A and B are the empirical constants, respectively.

When the finite rate/eddy dissipation model is used, both the Arrhenius and the eddy dissipation reaction rates are calculated, and the minimum value of these two contributions is defined as the net reaction rate.

2.2. Two-fluid CFD model

In the Two-fluid CFD model, both the gas and solid phases are treated as continuous inter-penetrating flows in an Eulerian framework. The gas is considered as the primary phase, whereas the solid phase is considered as the secondary phase. The phase-interaction terms, such as drag, collisions, and chemistry, are calculated using the kinetic theory of granular flows (KTGF), whereas the governing equations are given below [31–33].

The continuity equation for gas phase is given by Eq. (4).

$$\frac{\partial(\alpha_g \rho_g)}{\partial t} + \nabla \cdot (\alpha_g \rho_g \vec{u}_g) = S_{gs} \qquad (4)$$

The continuity equation for solid phase is given by Eq. (5).

$$\frac{\partial(\alpha_s \rho_s)}{\partial t} + \nabla \cdot (\alpha_s \rho_s \vec{u}_s) = S_{sg} = -S_{gs} \qquad (5)$$

The momentum equation for gas phase is given by Eq. (6).

$$\frac{\partial(\alpha_g \rho_g \vec{u}_g)}{\partial t} + \nabla \cdot (\alpha_g \rho_g \vec{u}_g \vec{u}_g) = -\alpha_g \nabla p + \alpha_g \rho_g \vec{g} - K(\vec{u}_g - \vec{u}_s)$$
$$+ S_{gs} \vec{u}_s + \nabla(\alpha_g \bar{\bar{\tau}}_g) \qquad (6)$$

The momentum equation for solid phase is represented by Eq. (7).

$$\frac{\partial(\alpha_s \rho_s \vec{u}_s)}{\partial t} + \nabla \cdot (\alpha_s \rho_s \vec{u}_s \vec{u}_s) = -\alpha_s \nabla p + \alpha_s \rho_s \vec{g} - K(\vec{u}_s - \vec{u}_g)$$
$$+ \nabla(\alpha_s \bar{\bar{\tau}}_s) + S_{sg} \vec{u}_s \qquad (7)$$

The energy equation for gas phase is given by Eq. (8).

$$\frac{\partial}{\partial t}(\alpha_g \rho_g H_g) + \nabla(\alpha_g \rho_g \vec{u}_g H_g) = \nabla(\lambda_g \nabla T_g) + h_{gs}(T_g - T_s) + S_{gs} H_s \qquad (8)$$

Table 3
Kinetic parameters for the heterogeneous reactions.

Reactions		Reaction rate (mol/(cm²·s))	A	E (kJ/mol)
R26	$C + CO_2 \rightarrow 2CO - 172.5$ kJ/mol	$\frac{d[C]}{dt} = -k_e[CO_2]$	3.42	130
R27	$C + H_2O \rightarrow CO + H_2 - 131.3$ kJ/mol	$\frac{d[C]}{dt} = -k_e[H_2O]$	3.42	130
R28	$C + 2H_2 \rightarrow CH_4 - 74.8$ kJ/mol	$\frac{d[C]}{dt} = -k_e[H_2]$	0.00342	130

The energy equation for solid phase is represented by Eq. (9).

$$\frac{\partial}{\partial t}(\alpha_s \rho_s H_s) + \nabla(\alpha_s \rho_s \vec{u}_s H_s) = \nabla(\lambda_s \nabla T_s) + h_{sg}(T_s - T_g) + S_{sg}H_s \quad (9)$$

where subscripts g and s represent gas phase and solid phase, respectively. Furthermore, subscripts gs and sg represent the interaction between the gas phase and solid phase. Additionally, $\vec{g}$, $\vec{u}$, and $\bar{\bar{\tau}}$ are the acceleration due to gravity, velocity vector, and second-order stress tensor, respectively, whereas p, α, ρ, and H are the pressure, volume fraction, density, and specific enthalpy, respectively. In addition, λ and h are the thermal conductivity and heat transfer coefficient, respectively, whereas K and S are the momentum exchange coefficient and mass source term due to the reactions, respectively.

The heat transfer coefficient is related to the Nusselt number and is given by Eq. (10).

$$h_{gs} = h_{sg} = \frac{6\lambda_g \alpha_g \alpha_s Nu_s}{d_s^2} \quad (10)$$

where Nu is Nusselt number.

For the heat transfer coefficient between the gas and solid phases, the Nusselt number proposed by Gunn [34] is given by Eq. (11).

$$Nu_s = (7 - 10\alpha_g + 5\alpha_g^2)(1 + 0.7Re_s^{0.2}Pr^{1/3})$$
$$+ (1.33 - 2.4\alpha_g + 1.2\alpha_g^2)Re_s^{0.7}Pr^{1/3} \quad (11)$$

For the heat transfer coefficient between the solid phases, the Nusselt number proposed by Tomiyama [35] is calculated using Eq. (12).

$$Nu_s = 2.0 + 0.15Re_s^{0.8}Pr^{0.5} \quad (12)$$

2.3. Computational domain and boundary conditions

In this study, the simulations are based upon the experimental setup used by Rapagnà et al. [36]. High temperature steam is used as the gasifying agent, whereas sand particles with average diameter of 348 μm and density of 2640 kg/m³ are used as the bed material to improve the fluidization and heat transfer effects. The biomass is crushed almond shell and is fed continuously to the fluidized bed b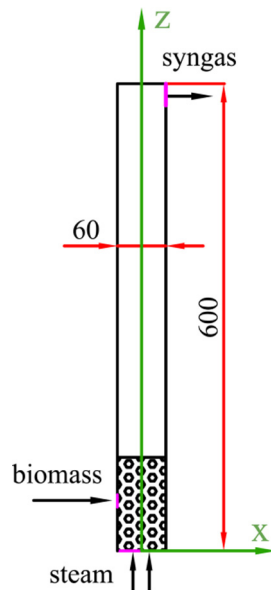y means of a tube. In simulation, the particles are supposed to be spherical and the size distribution is homogeneous. Due to this reason, the initial temperature of biomass is relatively high and is set to around 600 K in the simulation. The computational domain is simplified to 2D in the simulation. The geometry and coordinate system are schematically shown in Fig. 1, and the width of biomass inlet is 20 mm. The Z-direction represents the axial direction or the vertical (height) direction, whereas X-direction represents the radial or lateral direction.

Based on the mass fractions of C, H, and O and the mass fractions of cellulose, hemicellulose, and lignin, the mass fractions of LignC, LignH, and LignO are calculated. The physical and chemical properties of almond shell particles are given in Table 5.

For the simulation, the steam is introduced from the bottom of the bed and the atmospheric pressure boundary condition is used at the top of the bed. Additionally, the biomass is fed from the side of the bed. The biomass particles and the sand particles are all considered to be spherical in simulation, whereas the material properties for the solid phases are given in Table 6 [14,37].

where c_p is the specific heat.

The base case is modeled to validate the gasification model, whereas the boundary conditions for the base case are given in Table 7. Steam to biomass ratio (SBR) is defined as the ratio of steam mass flow (fed to the gasifier) to biomass mass flow (fed to the gasifier), and represents the rate of addition of steam in the gasification process. In the experiment, the minimum fluidization velocity for 0.348 mm sand particles with steam at gasification temperature is 0.075 m/s, and the value of u/u_{mf} is 2.44 corresponding to experimental condition. Hence, the velocity of steam is chosen as 0.183 m/s.

The interpenetrating effect of each phase can be accounted for by the drag model, which takes into account the exchange coefficient. Due to the huge difference between particles in volume fraction, the characteristic of this binary system is closer to the characteristic of the conventional gas–solid system. For the conventional gas–solid system, many studies [38,39] have shown that the Gidaspow drag model [40] is suitable for simulation involving a dense bubbling fluidized bed. Hence, in the simulation, Gidaspow drag model is used, and the gas–solid exchange coefficient is given by Eqs. (13) and (14).

when $\alpha_g > 0.8$,

$$K_{sg} = \frac{3}{4}C_D \frac{\alpha_s \alpha_g \rho_g |\vec{u}_s - \vec{u}_g|}{d_s} \alpha_g^{-2.65} \quad (13)$$

when $\alpha_g \leq 0.8$,

$$K_{sg} = 150\frac{\alpha_s(1 - \alpha_g)\mu_g}{\alpha_g d_s^2} + 1.75\frac{\alpha_s \rho_g |\vec{u}_s - \vec{u}_g|}{d_s} \quad (14)$$

where $C_D = \frac{24}{\alpha_g Re_s}[1 + 0.15(\alpha_g Re_s)^{0.687}]$.

Based on the kinetic theory of granular flow (KTGF), a constitutive model is obtained for the closure of governing relations. KTGF describes the particle collision based upon the restitution coefficient, which quantifies the elasticity of particle collision [41]. The value of unity for the restitution coefficient implies that the

Fig. 1. Schematic of the geometry and coordinate system.

Table 5
Physical and chemical properties of almond shell.

Parameter	Value	Parameter	Value
Moisture (wt.%)	7.9	LHV (kJ/kg)	18,350
Ash (wt.%)	1.16	Density (kg/m³)	1200
Cell (wt.%)	28.67	Particle size (μm)	1100
Hcell (wt.%)	27.68		
LignC (wt.%)	6.06		
LignH (wt.%)	4.83		
LignO (wt.%)	23.70		

Table 6
Material properties of the solid phases.

Property	$c_{p,shell}$	λ_{shell}	λ_{sand}	$c_{p,sand}$
Value	2380 J/(kg·K)	0.158 W/(m·K)	0.2 W/(m·K)	860 J/(kg·K)

Table 7
Boundary conditions for base case.

Property	u_{steam}	SBR	T_{wall}	T_{steam}	T_{shell}	T_{bed}
Value	0.183 m/s	1	1043 K	1043 K	600 K	1043 K

particle – particle collision is an absolutely elastic collision, whereas a value of zero shows that it is an absolutely inelastic collision. Some studies [42,43] have shown that the range of restitution coefficient is generally between 0.9 and 1 in a bubbling fluidized bed. Therefore, in the current work, the value of 0.95 is used.

In the simulation of gas–solid flow, two wall boundary slip conditions are generally used. One is the traditional "no slip" wall boundary condition, whereas the other is the Johnson and Jackson wall boundary condition [44]. Zhong et al. [45] reported that "no slip" wall boundary condition was more suitable for simulating a binary system in a fluidized bed. Therefore, "no slip" wall boundary condition is adopted in the current work.

When TFM is used for the simulation, the grid size should be much smaller than the physical dimensions of the computational domain. Meanwhile, it should also be bigger than the particle diameter, which ensures that the solid phase can be treated as a continuous flow in an Eulerian framework. Many studies have been done about the effect of grid size on the simulation results. A coarse grid can lead to an over-prediction of the solid expansion height of the bed [33]. However, when the mesh is further refined there is no improvement in capturing homogeneous expansion, and the numerical results agree well with the experimental data when the grid size is about 10 times the particle diameter [39]. In this study, sand particles with average diameters of 348 μm and almond particles with diameters of 1100 μm are used for bed materials. Considering the computational domain with 60 mm width, hence, a grid size of 5 mm is chosen in the current work.

3. Results and discussion

3.1. Model validation

3.1.1. Stationary condition

The changes in syngas composition and phase temperature with time are used to confirm the stability of simulation. The instantaneous mole fraction of syngas composition at the outlet of the bed for the base case is shown in Fig. 2. At the beginning of simulation, the fluidized bed is filled with the high temperature steam, due to which, the mole fraction of H_2O is unity and the composition values of all other gases are zero. With the increase in time, the biomass enters the bed, where the gasification reaction takes place. When the produced syngas reaches the outlet of the bed, the mole fraction of H_2O decreases whereas the composition values of other gases increase.
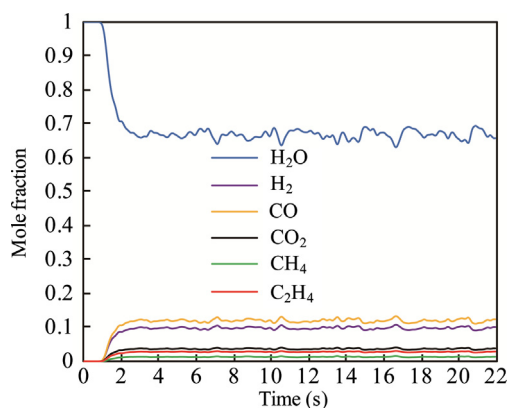
Fig. 3 presents the instantaneous gas phase temperature at the outlet of the bed and the biomass temperature at the height of 0.08 m. It is observed that the gas phase temperature decreases, whereas the biomass temperature increases with the increase in simulation time (from 0 s to 2 s). After 15 s, the syngas composition and the phase temperature reach a quasi-steady state, due to which, the time-averaged variables are computed between 15 s to 25 s.

3.1.2. Instantaneous distribution

Fig. 4 shows the instantaneous volume fraction and temperature distributions at 17 s. It can be seen that the biomass volume fraction is far less than that of the sand volume fraction. This is because of the existence of fast pyrolysis reactions. In the sand volume fraction distribution, the area corresponding to small volume fraction is of the bubble. Small bubbles are generated at the bottom of the bed, which rise and grow larger in size by coalescing. Hence, large bubbles are formed at the top of the bed, as shown in Fig. 4. The uniform distribution of bubbles shows that the steady fluidization is achieved.

In the region of dense solid phase bed, due to the heat exchange between the gas and solid phases, the gas phase temperature has the same value as the temperature of the inlet steam. Above this

Fig. 2. Changes in the outlet syngas composition with time.
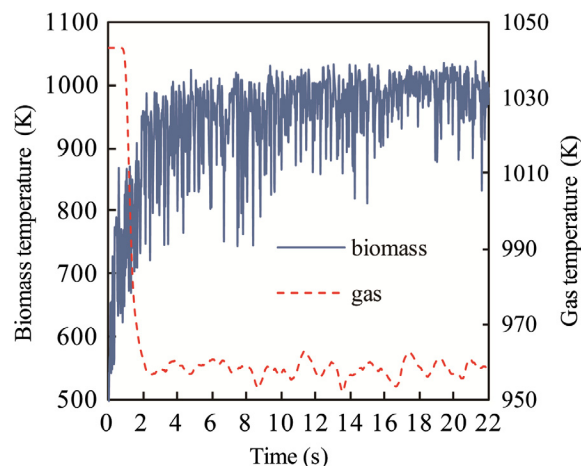
Fig. 3. Changes in the outlet gas phase temperature and biomass temperature at the height of 0.08 m.
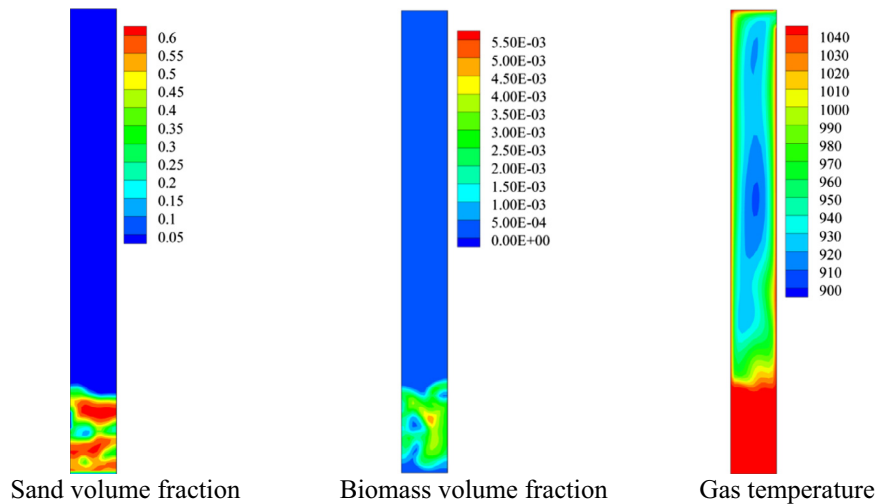
Fig. 4. Instantaneous volume fractions and temperature distributions of various phases.

region, the temperature lies within the range of 900–950 K, which is lower than the inlet steam temperature (1043 K). This is due to the two endothermic reactions R29 and R30. This shows that the gasification reaction is endothermic when the gasifying agent is pure steam, which is consistent with the results reported in some previous studies [46]. Since the wall temperature is set to be the same as the temperature of the inlet steam, the gas phase temperature in the region near the wall is slightly higher than the temperature in the central region due to the heating.

Due to the existence of secondary pyrolysis, the tar at the outlet of the bed is determine to consist of C_2H_5OH, CH_3HCO, CH_3OH, CH_2O, $C_6H_6O_3$, and CH_3COCH_3. Fig. 5 shows the distributions of instantaneous mole fractions of these tar components. In the gas phase, the gas composition consists of non-condensable gases, steam, and tar. The inlet of biomass is on the left of the bed. Hence, the pyrolysis reactions take place immediately on the left of the bed, which causes the mole fraction of syngas higher in this region. The lateral asymmetry can be found at the bottom of the bed, as shown in Fig. 5. In the freeboard of the fluidized bed, for C_2H_5OH, CH_3HCO, CH_3OH, and CH_2O, the change in distribution of mole fractions is not evident along the vertical (height) direction.

However, for $C_6H_6O_3$ and CH_3COCH_3, the mole fraction decreases with the increase in height because they take part in the secondary pyrolysis reaction through reactions R16 and R17.

Fig. 6 shows the distributions of instantaneous reaction rates of different reactions, whereas the units of the reaction rate are kmol/(m^3·s). The reaction rate of R12 is the slowest among all primary pyrolysis reactions, whereas reaction R25 is one of the secondary pyrolysis reactions. Reactions R29, R30, and R31₊ belong to the homogenous gas phase reactions. Reaction R31₊ is the forward reaction of water gas shift reaction, whereas the reaction rate of R31₊ is higher than that of the backward reaction. It can be seen that the reaction rates of primary pyrolysis reactions are several orders of magnitude higher than the others. Hence, it is somewhat reasonable that the primary pyrolysis reactions are considered as the instantaneous devolatilization reactions. The primary pyrolysis reactions and the secondary pyrolysis reactions take place in the region of dense solid phase bed, and therefore, the height of the fluidized bed has no effect on the pyrolysis products. However, homogeneous gas phase reaction rates change with the height of the bed, due to which, the height of the bed has obvious effect on the syngas composition. In the freeboard of the bed, with the
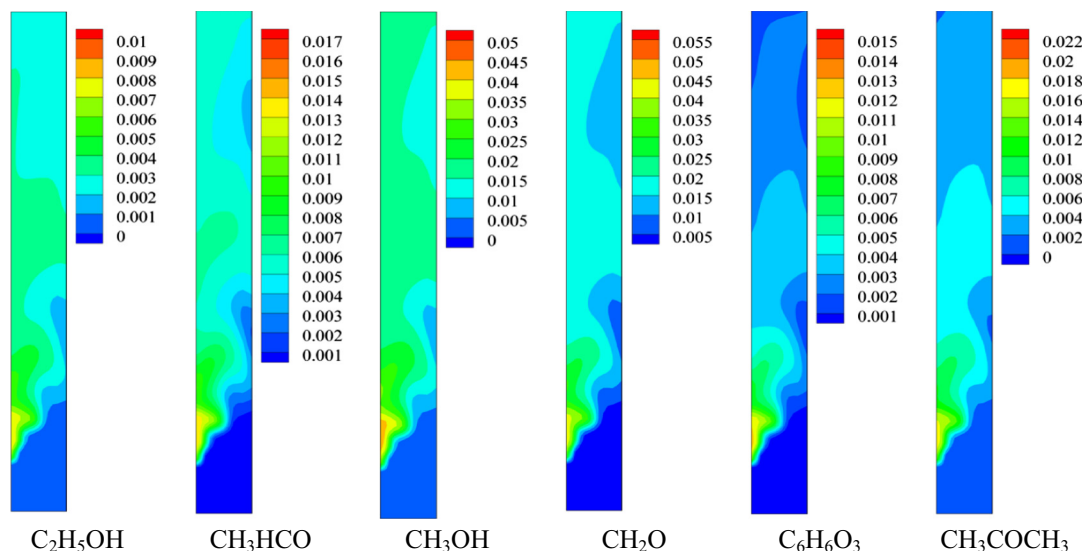

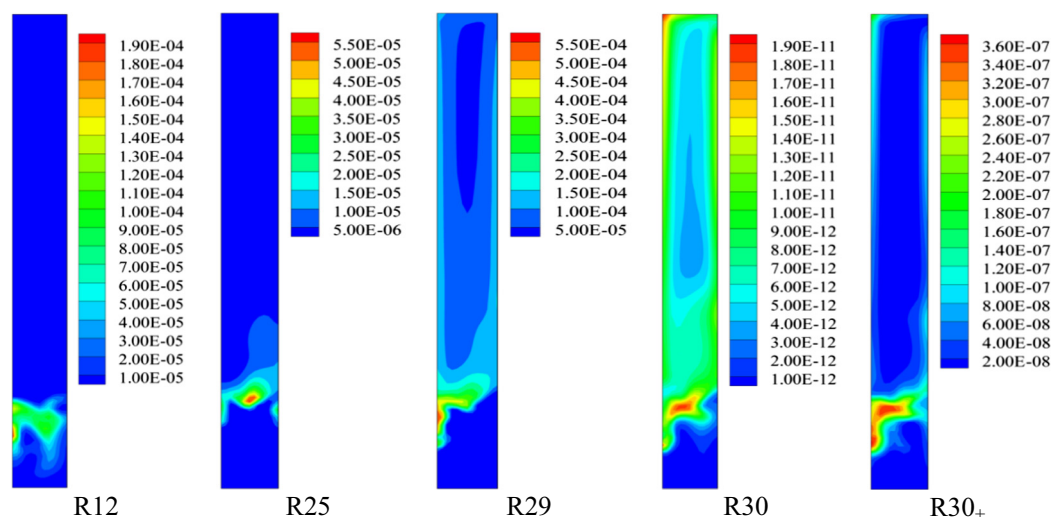**Fig. 5.** Distributions of instantaneous mole fraction of tar.

Fig. 6. The distribution of reaction rates of various reactions.

decrease in concentration and temperature of gases, the reaction rates of gas phase reactions become smaller.

3.1.3. Time-averaged values

The comparison between the simulation results and experimental data for volume fractions of four gas components at the outlet of the bed is shown in Fig. 7, and the experimental data also come from the same reference [36]. The volume fraction of an individual component of gas is defined as the volume of individual component divided by the total volume of dry syngas, which does not include tar components. In the experiment, the small-molecule hydrocarbons are not easy to separate, due to which, they are normally lumped together in calculation as CH_4. In this study, the small-molecule hydrocarbons include CH_4 and C_2H_4, and are all lumped together as CH_4. Fig. 7 shows that the predicted volume fractions of CO_2 and CH_4 agree well to the experimental data, except for H_2 and CO which deviate slightly from the experimental data.

When the combustible components of syngas are CO, H_2, and CH_4, the lower heating value (LHV) of the syngas is calculated using Eq. (15).

$$LHV = 12.64\varphi_{CO} + 10.8\varphi_{H_2} + 35.8\varphi_{CH_4} \tag{15}$$

where the unit of LHV is MJ/N m^3. φ is the corresponding molar fraction of combustible gas species in the syngas, which is free from steam and tar.
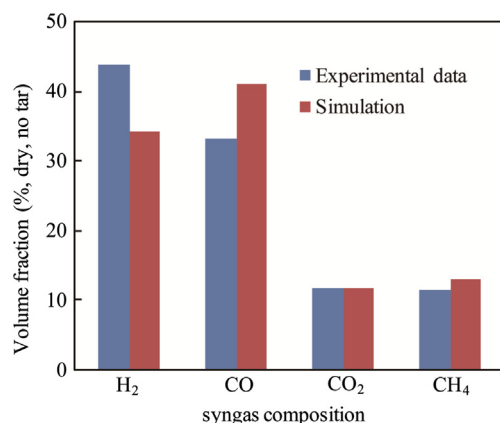

Fig. 7. Comparison between the experimental and predicted data for syngas components.

The comparison between the experimental and predicted results for tar content, char yield, and LHV of syngas is shown in Table 8. The tar content is calculated by dividing the tar mass by the volume of dry syngas, and is given in units of g/N m^3. The char yield is the produced char mass per kilogram of raw biomass, and has the unit of gram (g). In the experiment, the tar is usually obtained through the sampling device with the adsorbent. Some studies [47] show that the tar yield varies with different sampling devices and adsorbents. Therefore, it is reasonable to believe that the experimental data of tar content is always smaller than the actual values. The value of predicted tar content is higher than the experimental data, though the deviation is not more than 50%. The char can be blown out in the experiment, due to which, the experimental data of char yield is also smaller than the actual value. Meanwhile, the inaccuracy of kinetic parameters may be the second reason that low char conversion can be found in simulation. In this study, the value of predicted char yield is also higher than the experimental data, though the deviation is not more than 50%. The predicted value is slightly higher than the experimental result.

Based on the analysis of syngas compositions, tar content, char yield, and LHV of syngas, the proposed steam gasification kinetic model is proved reasonable and accurate.

3.2. Effect of temperature

While studying the effect of gasification temperature on the gasification results, the value of SBR is fixed at 1, and that of the wall temperature is set to be the same as the temperature of the inlet steam. The temperatures of gasification are 950 K, 1000 K, 1043 K, and 1100 K, respectively.

The time-averaged distributions of the mole fractions of CO and H_2 in the gas phase at different temperatures are shown in Figs. 8 and 9, respectively. In the gas phase, the gas components consist of non-condensable gases, steam, and tar components.

Table 8
Comparison of the predicted and experimental values of tar content, char yield, and LHV of gas.

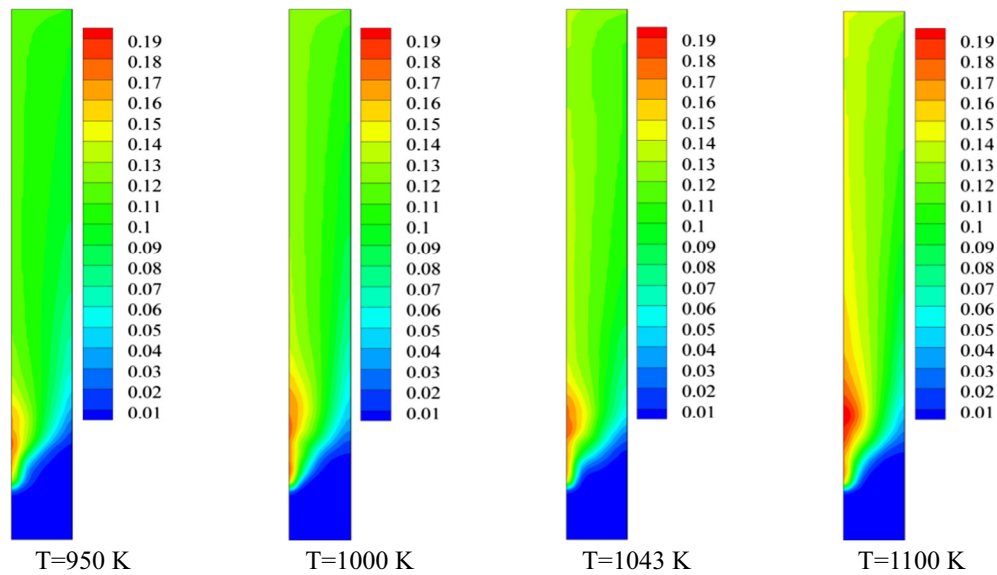| Parameter	Tar content (g/N m^3)	Char yield (g)	LHV of the gas (MJ/N m^3)
Experimental data	43	102	13
Simulation result	65	142	13.57

Fig. 8. Time-averaged distributions of mole fractions of CO at different temperatures.
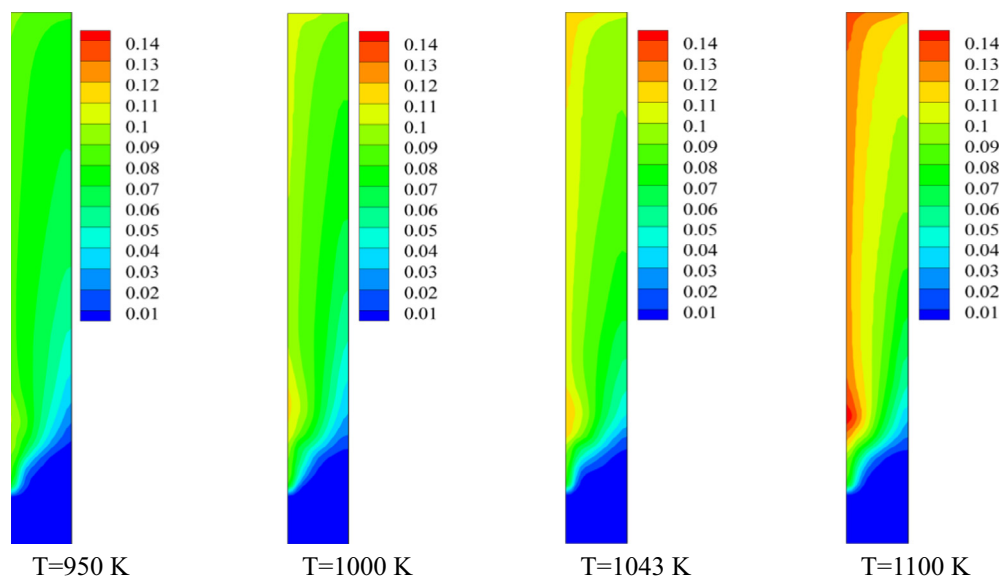

Fig. 9. Time-averaged distributions of mole fractions of H_2 at different temperatures.

With increase in temperature, the mole fraction of H_2 increases more obviously than CO. Hence, it is beneficial to obtain hydrogen in the process of gasification by increasing the gasification temperature.

he effect of gasification temperature on syngas composition at the outlet of the bed is shown in Fig. 10. In the dry syngas without tar, the mole fraction of H_2 increases significantly as the temperature increases, whereas the mole fractions of CO_2 and CH_4 show a decreasing trend, which is in agreement to some experimental results reported in literature [36,48].

Due to the reason that the mole fraction of CH_4 decreases obviously with the increase in temperature, meanwhile, the coefficient corresponding to the mole fraction of CH_4 (calculated from Eq. (15)) is the largest. Hence, with the increase in temperature, the LHV of syngas decreases.

The effect of gasification temperature on tar content and char yield is shown in Fig. 11. The tar content decreases with the

increase in temperature, which is consistent with the experimental results [36]. The value changes from 88.6 g/N m^3 at 950 K to 53.1 g/N m^3 at 1100 K. The char yield increases slightly with the increase in temperature, which is also consistent with some previously reported data [49]. Additionally, it is related to the coking characteristics of the biomass at high gasification temperatures.

Fig. 12 shows the effect of gasification temperature on the mass fractions of tar components. As the temperature increases, the reaction rates of primary pyrolysis reactions and secondary pyrolysis reactions increase. The tar components of CH_3HCO, CH_2O, C_2H_5OH, and CH_3OH do not take part in the subsequent reactions after the primary pyrolysis reactions. Therefore, the mass fractions of CH_3HCO, CH_2O, C_2H_5OH, and CH_3OH increase obviously. Since the tar components of $C_6H_6O_3$ and CH_3COCH_3 continue to take part in the secondary pyrolysis reaction, the mass fractions of these components decrease accordingly.
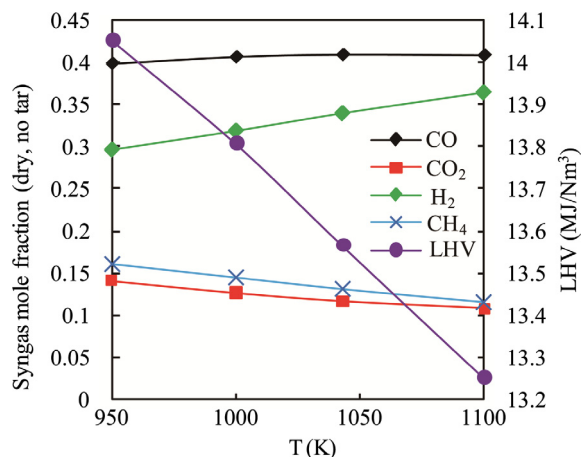
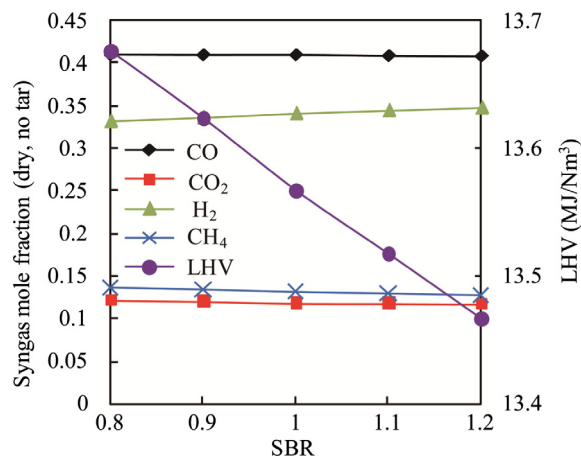**Fig. 10.** Effect of gasification temperature on syngas composition and LHV.

Fig. 13. Effect of SBR on syngas composition and LHV.
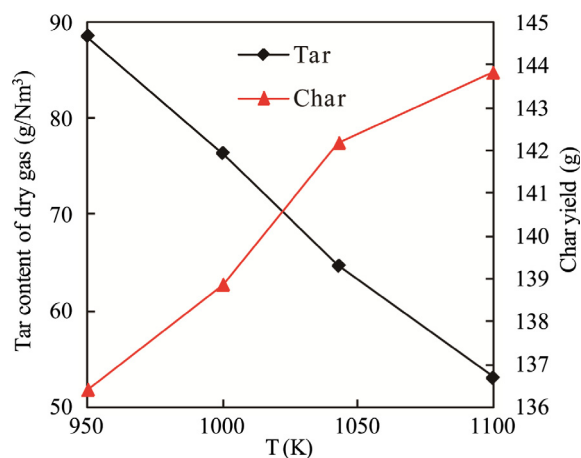

Fig. 11. Effect of gasification temperature on the tar content and char yield.
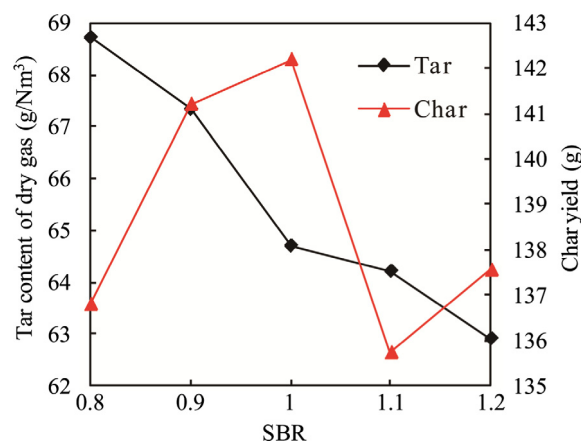

Fig. 14. Effect of SBR on tar content and char yield.
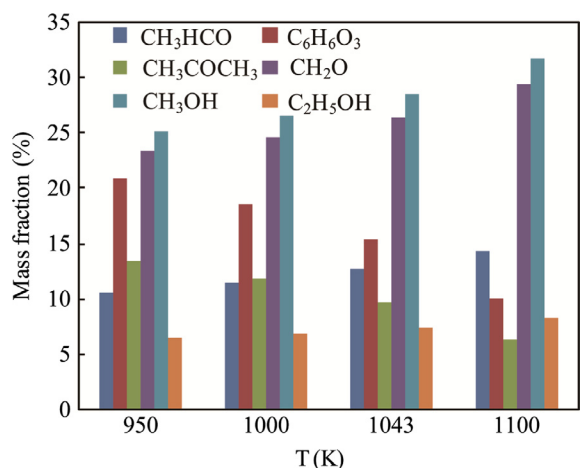

Fig. 12. Effect of gasification temperature on the mass fraction of tar components.
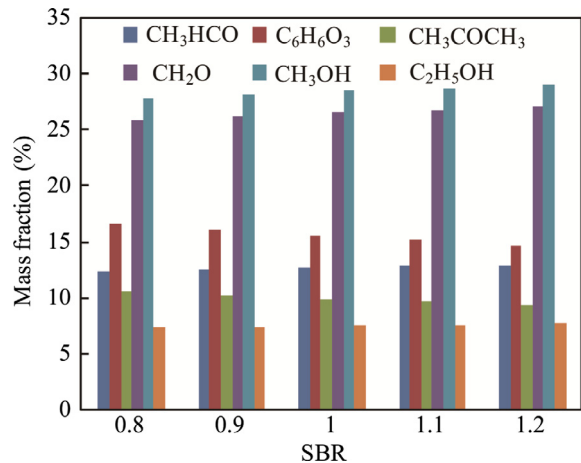

Fig. 15. Effect of SBR on mass fractions of tar components.

3.3. Effect of SBR

While studying the effect of SBR on the gasification results, the gasification temperature is fixed at 1043 K, whereas the SBR values are changed to 0.8, 0.9, 1, 1.1, and 1.2, respectively. For different cases, the steam mass flow rate is fixed and the SBR changes based on the change of biomass mass flow rate, which eliminates the impact of extent of reaction on syngas composition because of the same residence time of the gas phase through the bed.

Fig. 13 shows the variation of syngas components at the outlet of the bed with SBR, whereas the syngas is free from steam and tar. Since a larger value of SBR favors the Reactions R29, R30, and R31+, the mole fraction of H_2 increases with the increase in SBR, which is

consistent to results obtained in some previous studies [36,50]. However, the change of mole fractions of CH_4, CO, and CO_2 is not obvious with the increase in SBR. The result shows that the effect of SBR on syngas composition is not evident. Hence, the effect of SBR on LHV is also not evident, as shown in Fig. 13, whereas the LHV decreases slightly with the increase in SBR.

The effect of SBR on tar content and char yield is shown in Fig. 14. The tar content decreases from 68.7 g/N m^3 at SBR of 0.8 to 62.9 g/N m^3 at SBR of 1.2, however, the decrease in tar content is not obvious. Moreover, the change in mass fractions of tar components is also not noticeable with the increase in SBR, which can be seen in Fig. 15. In addition, the minimum char yield is 135.7 g at SBR of 1.1, while the maximum char yield is 142.2 g at SBR of 1. From Fig. 14, it can be seen that the SBR and char yield are not correlated monotonously. Furthermore, some studies [49] also showed that the char yield is weakly related to SBR.

4. Conclusions

In the present work, a multi-composition biomass steam gasification kinetic model along with a detailed multi-step pyrolysis scheme was developed, and simulations were carried out based on two-fluid model along with the kinetic theory of granular flow. Based on the base case, the gasification model was validated by comparing the predicted results and experimental data for syngas compositions, tar content, and char yield. The results showed that the proposed kinetic model is suitable for the simulation of steam gasification process, which can also predict the tar composition.

The effect of gasification temperature (950 K, 1000 K, 1043 K, and 1100 K) and SBR (0.8, 0.9, 1, 1.1, and 1.2) on predicted results was also studied. The gasification temperature had an evident influence on the predicted results. As the temperature increased, the mole fraction of H_2 increased drastically, while those of CH_4 and CO_2 decreased obviously. The tar content decreased whereas the char yield increased with the increase in temperature. The effect of SBR on syngas composition, tar content, char yield, and tar composition was not obvious. The tar content decreased slightly as the SBR increased, while the char yield did not change monotonously with SBR.

References

[1] A. Gómez-Barea, B. Leckner, Modeling of biomass gasification in fluidized bed, Prog. Energy Combust. Sci. 36 (2010) 444–509.

[2] C. Loha, S. Gu, W.J. De, P. Mahanta, P.K. Chatterjee, Advances in mathematical modeling of fluidized bed gasification, Renew. Sustain. Energy Rev. 40 (2014) 688–715.

[3] T.Y. Ahmed, M.M. Ahmad, S. Yusup, A. Inayat, Z. Khan, Mathematical and computational approaches for design of biomass gasification for hydrogen production: a review, Renew. Sustain. Energy Rev. 16 (2012) 2304–2315.

[4] M. Puig-Arnavat, J.C. Bruno, A. Coronas, Review and analysis of biomass gasification models, Renew. Sustain. Energy Rev. 14 (2010) 2841–2851.

[5] D. Baruah, D.C. Baruah, Modeling of biomass gasification: a review, Renew. Sustain. Energy Rev. 39 (2014) 806–815.

[6] M.J.H. Khan, M.A. Hussain, Z. Mansourpour, N. Mostoufi, N.M. Ghasem, E.C. Abdullah, CFD simulation of fluidized bed reactors for polyolefin production – a review, J. Ind. Eng. Chem. 20 (2014) 3919–3946.

[7] P. Ranganathan, S. Gu, Computational fluid dynamics modelling of biomass fast pyrolysis in fluidised bed reactors, focusing different kinetic schemes, Bioresour. Technol. 213 (2016) 333–341.

[8] C. Loha, H. Chattopadhyay, P.K. Chatterjee, Three dimensional kinetic modeling of fluidized bed biomass gasification, Chem. Eng. Sci. 109 (2014) 53–64.

[9] E. Esmaili, N. Mahinpey, E. Mostafavi, An extensive simulation of coal gasification in bubbling fluidized bed: integration of hydrodynamics into reaction modelling, Can. J. Chem. Eng. 92 (2014) 1714–1724.

[10] H. Liu, R.J. Cattolica, R. Seiser, CFD studies on biomass gasification in a pilot-scale dual fluidized-bed system, Int. J. Hydrogen Energy 41 (2016) 11974–11989.

[11] X. Ku, T. Li, T. Løvås, CFD–DEM simulation of biomass gasification with steam in a fluidized bed reactor, Chem. Eng. Sci. 122 (2015) 270–283.

[12] T.M. Ismail, M. Abd El-Salam, E. Monteiro, A. Rouboa, Eulerian – Eulerian CFD model on fluidized bed gasifier using coffee husks as fuel, Appl. Therm. Eng. 106 (2016) 1391–1402.

[13] Q. Xue, R.O. Fox, Multi-fluid CFD modeling of biomass gasification in polydisperse fluidized-bed gasifiers, Powder Technol. 254 (2014) 187–198.

[14] S. Gerber, F. Behrendt, M. Oevermann, An Eulerian modeling approach of wood gasification in a bubbling fluidized bed reactor using char as bed material, Fuel 89 (2010) 2903–2917.

[15] Q. Xue, T.J. Heindel, R.O. Fox, A CFD model for biomass fast pyrolysis in fluidized-bed reactors, Chem. Eng. Sci. 66 (2011) 2440–2452.

[16] K. Umeki, K. Yamamoto, T. Namioka, K. Yoshikawa, High temperature steam-only gasification of woody biomass, Appl. Energy 87 (2010) 791–798.

[17] S. Fremaux, S.-M. Beheshti, H. Ghassemi, R. Shahsavan-Markadeh, An experimental study on hydrogen-rich gas production via steam gasification of biomass in a research-scale fluidized bed, Energy Convers. Manage. 91 (2015) 427–432.

[18] R. Eliseo, C. Alberto, F. Tiziano, F. Alessio, M. Gabrele, P. Sauro, S. Samuele, Chemical kinetics of biomass pyrolysis, Energy Fuels 22 (2008) 4292–4300.

[19] P. Mellin, E. Kantarelis, W. Yang, Computational fluid dynamics modeling of biomass fast pyrolysis in a fluidized bed reactor, using a comprehensive chemistry scheme, Fuel 117 (2014) 704–715.

[20] T. Hosoya, H. Kawamoto, S. Saka, Cellulose–hemicellulose and cellulose–lignin interactions in wood pyrolysis at gasification temperature, J. Anal. Appl. Pyrol. 80 (2007) 118–125.

[21] A. Anca-Couce, R. Mehrabian, R. Scharler, I. Obernberger, Kinetic scheme of biomass pyrolysis considering secondary charring reactions, Energy Convers. Manage. 87 (2014) 687–696.

[22] J. Mabrouki, M.A. Abbassi, K. Guedri, A. Omri, M. Jeguirim, Simulation of biofuel production via fast pyrolysis of palm oil residues, Fuel 159 (2015) 819–827.

[23] Q. Xue, D. Dalluge, T.J. Heindel, R.O. Fox, R.C. Brown, Experimental validation and CFD modeling study of biomass fast pyrolysis in fluidized-bed reactors, Fuel 97 (2012) 757–769.

[24] M. Calonaci, R. Grana, E. Barker Hemings, G. Bozzano, M. Dente, E. Ranzi, Comprehensive kinetic modeling study of bio-oil formation from fast pyrolysis of biomass, Energy Fuels 24 (2010) 5727–5734.

[25] G. Cheng, Q. Li, F. Qi, B. Xiao, S. Liu, Z. Hu, P. He, Allothermal gasification of biomass using micron size biomass as external heat source, Bioresour. Technol. 107 (2012) 471–475.

[26] L. Fagbemi, L. Khezami, R. Capart, Pyrolysis products from different biomasses: application to the thermal cracking of tar, Appl. Energy 69 (2001) 293–306.

[27] J. Blondeau, H. Jeanmart, Biomass pyrolysis at high temperatures: prediction of gaseous species yields from an anisotropic particle, Biomass Bioenerg. 41 (2012) 107–121.

[28] C. Di Blasi, Combustion and gasification rates of lignocellulosic chars, Prog. Energy Combust. Sci. 35 (2009) 121–140.

[29] D.M. Snider, S.M. Clark, P.J. O'Rourke, Eulerian-Lagrangian method for three-dimensional thermal reacting flow with application to coal gasifiers, Chem. Eng. Sci. 66 (2011) 1285–1295.

[30] J. Xie, W. Zhong, B. Jin, Y. Shao, H. Liu, Simulation on gasification of forestry residues in fluidized beds by Eulerian-Lagrangian approach, Bioresour. Technol. 121 (2012) 36–46.

[31] J. Xie, W. Zhong, B. Jin, Y. Shao, H. Liu, Three-dimensional Eulerian-Eulerian modeling of gaseous pollutant emissions from circulating fluidized-bed combustors, Energy Fuels 28 (2014) 5523–5533.

[32] N. Couto, V. Silva, E. Monteiro, S. Teixeira, R. Chacartegui, K. Bouziane, P.S.D. Brito, A. Rouboa, Numerical and experimental analysis of municipal solid wastes gasification process, Appl. Therm. Eng. 78 (2015) 185–195.

[33] J. Chen, G. Yu, B. Dai, D. Liu, L. Zhao, CFD simulation of a bubbling fluidized gasifier using a bubble-based drag model, Energy Fuels 28 (2014) 6351–6360.

[34] D.J. Gunn, Transfer of heat or mass to particles in fixed and fluidised beds, Int. J. Heat Mass Transf. 21 (1978) 467–476.

[35] A. Tomiyama, Struggle with computational bubble dynamics, Multiphase Sci. Technol. 10 (1998) 369–405.

[36] S. Rapagnà, N. Jand, A. Kiennemann, P.U. Foscolo, Steam-gasification of biomass in a fluidised-bed of olivine particles, Biomass Bioenerg. 19 (2000) 187–197.

[37] R. Radmanesh, J. Chaouki, C. Guy, Biomass gasification in a bubbling fluidized bed reactor:experiments and modeling, AIChE J. 52 (2006) 4258–4272.

[38] C. Loha, H. Chattopadhyay, P.K. Chatterjee, Assessment of drag models in simulating bubbling fluidized bed hydrodynamics, Chem. Eng. Sci. 75 (2012) 400–407.

[39] P.C. Sande, S. Ray, Mesh size effect on CFD simulation of gas-fluidized Geldart A particles, Powder Technol. 264 (2014) 43–53.

[40] J. Ding, D. Gidaspow, A bubbling fluidization model using kinetic theory of granular flow, AIChE J. 36 (1990) 523–538.

[41] M. Askarishahi, M.-S. Salehi, A. Molaei Dehkordi, Numerical investigation on the solid flow pattern in bubbling gas–solid fluidized beds: effects of particle size and time averaging, Powder Technol. 264 (2014) 466–476.

[42] V. Verma, N.G. Deen, J.T. Padding, J.A.M. Kuipers, Two-fluid modeling of three-dimensional cylindrical gas–solid fluidized beds using the kinetic theory of granular flow, Chem. Eng. Sci. 102 (2013) 227–245.

[43] F. Taghipour, N. Ellis, C. Wong, Experimental and computational study of gas–solid fluidized bed hydrodynamics, Chem. Eng. Sci. 60 (2005) 6857–6867.

[44] P.C. Johnson, R. Jackson, Frictional-collisional constitutive relations for granular materials with application to plane shearing, J. Fluid Mech. 176 (1987) 67–93.

[45] H. Zhong, X. Lan, J. Gao, Y. Zheng, Z. Zhang, The difference between specularity coefficient of 1 and no-slip solid phase wall boundary conditions in CFD simulation of gas–solid fluidized beds, Powder Technol. 286 (2015) 740–743.

[46] C. Loha, H. Chattopadhyay, P.K. Chatterjee, Thermodynamic analysis of hydrogen rich synthetic gas generation from fluidized bed gasification of rice husk, Energy 36 (2011) 4063–4071.

[47] S. Osipovs, Use of two different adsorbents for sampling tar in gas obtained from peat gasification, Int. J. Environ. Anal. Chem. 89 (2009) 871–880.

[48] C. Loha, H. Chattopadhyay, P.K. Chatterjee, Energy generation from fluidized bed gasification of rice husk, J. Renewable Sustain. Energy 5 (2013) 043111.

[49] X. Li, J.R. Grace, A.P. Watkinson, C.J. Lim, A. Ergudenler, Equilibrium modeling of gasification: a free energy minimization approach and its application to a circulating fluidized bed coal gasifier, Fuel 80 (2001) 195–207.

[50] M.K. Karmakar, A.B. Datta, Generation of hydrogen rich gas through fluidized bed gasification of biomass, Bioresour. Technol. 102 (2011) 1907–1913.